Inversion of sound-speed and density profiles in deep ocean sediments

N. R. Chapman, S. Levy, K. Stinson, et al.

Citation: The Journal of the Acoustical Society of America **79**, 1441 (1986); doi: 10.1121/1.393743
View online: https://doi.org/10.1121/1.393743
View Table of Contents: https://asa.scitation.org/toc/jas/79/5
Published by the Acoustical Society of America

Inversion of sound-speed and density profiles in deep ocean sediments

N. R. Chapman
Defence Research Establishment Pacific, FMO, Victoria, British Columbia, V0S 1B0, Canada

S. Levy, K. Stinson, I. F. Jones, B. T. Prager, and D. W. Oldenburg
Inverse Theory and Applications Incorporated, #241 7080 River Road, Richmond, British Columbia, V6X 1A5, Canada

(Received 3 January 1985; accepted for publication 21 January 1986)

Wide-angle seismic reflections obtained in a deep ocean environment are analyzed to obtain estimates of the sound-speed profile and density contrasts in the surficial sediment layers. The analysis begins with a new deconvolution technique based on autoregressive modeling, which is used to deconvolve the bubble-pulse signature from the data. Sound-speed profiles are then obtained by inverting the identified arrivals by first treating them as reflection events, and then as refraction events. The first inversion was performed twice, once using a Backus–Gilbert approach (to produce a smooth model) and once using a linear programming method (to produce a blocky model). For the refraction inversion, the Garmany $p - \tau$ method was used. Finally, the offset-dependent phase shifts of supercritically reflected arrivals were estimated using the complex Karhunen–Loeve transform. These phase shifts were used with Rayleigh's equation in a new inversion scheme to obtain density and sound-speed contrasts in the shallow sediments.

PACS numbers: 43.30.Pc, 43.60.Pt, 43.20.Bi, 92.10.Vz

INTRODUCTION

Determination of both sound-speed and density profiles for the surficial sediment layers in a deep ocean environment is a prerequisite for the construction of realistic models pertaining to acoustic interaction with the ocean bottom. In a previous study, Chapman *et al.*[1] described an L_1 deconvolution processing technique and a simple model by which the sound-speed gradient in the surficial sediments was determined from a suite of recordings of wide-angle seismic reflections at varying source–receiver offset. This determination involved the assumptions that (a) the sound-speed gradient in the sediment layer of interest remained constant with depth and (b) the analyzed arrivals corresponded to waves which had been refracted within the constant gradient layer. Hence, an expression describing the different arrival times could be used to determine the sound-speed gradient. This type of model has also been used by Dicus and Anderson,[2] Santaniello *et al.*,[3] and Chapman[4] to analyze bottom reflection data.

In this paper, we present a new method for bubble-pulse deconvolution and a different approach to the inversion of ocean bottom reflection data in which there is no need to invoke the assumptions made by other workers. We first describe an autoregressive technique for the deconvolution of seismic data which is based on the spectral characteristics of the full source wavelet impinging on the ocean bottom. This technique does not require *a priori* knowledge of the wavelet signature. Three inversion techniques are then applied to construct a one-dimensional sound-speed model: In the first two methods the analyzed arrivals are treated as reflection data, while in the last method, the arrivals are treated as refractions. The sound-speed model is assumed to be either a layered or a continuous function of depth (as the different techniques require).

Following the analysis of the sound-speed profile, we use the complex Karhunen–Loeve transform to determine the trace to trace phase differential of certain events. This phase information is then inverted to obtain the density and sound-speed contrast across an internal sediment layer. That is, we first estimate the offset-dependent phase shifts for a number of supercritical reflection arrivals, assumed to be first multiple reflections from an internal layer, and then use this information to estimate both the sound speed and density of the sediment layers.

Some of the techniques used in this work are in widespread use in exploration geophysics for the analysis of seismic data. As will be shown in this paper, they provide powerful analysis methods which make few assumptions about the sub-bottom profile. However, these methods have been largely overlooked by the underwater acoustics community in processing ocean bottom reflection data, and therefore more detailed descriptions of the techniques have been included in the Appendices.

I. DATA ACQUISITION

The data set analyzed in this paper was obtained in a wide-angle seismic reflection experiment carried out at a site in the Alaskan Abyssal Plain where the sea floor is uniformly flat, with an average depth of 3625 m over the track of the shot run. The ocean bottom in this region of the plain consists of turbidite layers, and the near surface sediments are composed of unconsolidated silty deposits. In the acquisition stage, small explosive charges (0.82 kg) were deployed at an average depth of 190 m, and a hydrophone suspended at 415 m was used to record the ocean bottom reflections at offsets ranging from 2–40 km.

The data shown in Fig. 1 were sampled at 0.667 ms. It should be noted that in all plots of the seismic sections (un-

 0001-4966/86/051441-16$00.80

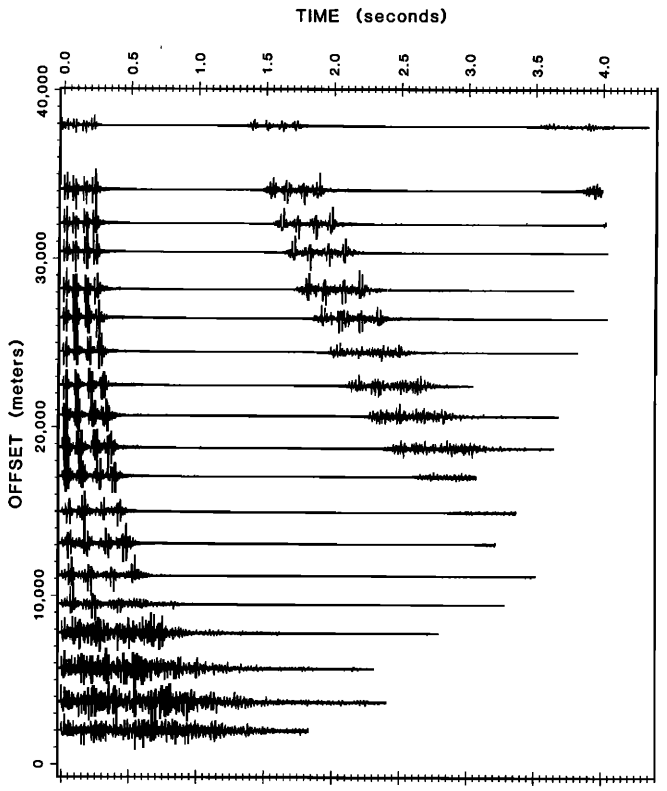

FIG. 1. The original data, sampled at 0.667 ms, plotted in reduced time using a sound speed of 1500 m/s, aligned on the first water bottom reflection.

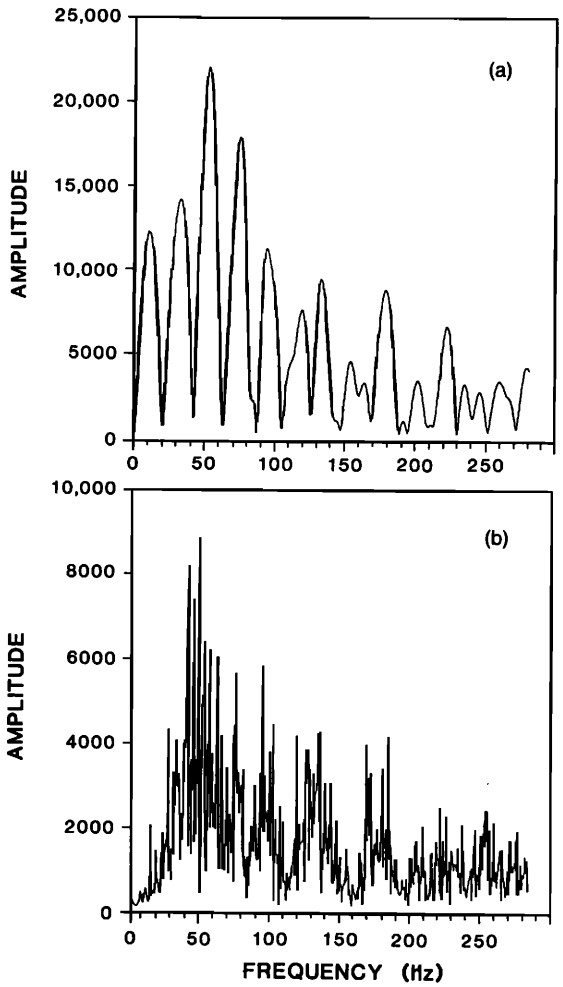

FIG. 2. (a) The spectrum of the direct arrival. Note the notches at 20-Hz spacing due to the ghost interference. (b) The spectrum of the first bottom bounce arrival. Note the bubble pulse notches at about 50-Hz spacing.

less otherwise stated) a reduced-time scale is used in which "zero-time" is offset dependent and is set at the sample point corresponding to the first reflection from the sea floor for the given offset. In the actual analyses, the time values assigned to the first bottom reflection correspond to a hyperbolic moveout expressed by $T^2 = (2Z_W/V_W)^2 + X^2/V_W^2$, with Z_W the water depth (3625 m), V the sound speed in the water (1500 m/s), and X the source–receiver offset.

In those records in Fig. 1 with offsets greater than 18 km, a second group of later reflection arrivals is apparent on each trace. These are the first water surface multiples (second bottom bounce) of the preceding group of arrivals. These data will be used in the inversion of phase-shift information to recover density ratios and sound speeds.

II. DECONVOLUTION/DEBUBBLING OF MARINE REFLECTION DATA

When single-source seismic experiments are carried out in a marine environment, the presence of the bubble-pulse train associated with both the source and its water surface reflection (ghost) severely limits the resolution obtainable. Detailed analysis of seismograms recorded under these conditions is largely improved if the ghost and the bubble-pulse train have been previously removed. In the experiments reported here, the effect of ghost interference in the bottom reflections has been greatly reduced by careful design of the source–receiver geometry. As for the bubble pulse, a number of debubbling techniques have been suggested in the geophysical literature and potentially could have been used (e.g., Wood *et al.*[5]; Levy and Clowes[6]). However, most of these either require a wavelet signature or the calculation of one in the debubbling process. Here, we present a new scheme which uses only the spectral characteristics of the bubble-pulse train.

It is well known that both the ghost and the bubble-pulse train produce a strong periodic modulation in the spectrum of the observed seismograms. This is clearly seen in the amplitude spectrum of the direct arrival from the seismogram corresponding to a source–receiver offset of 2 km [see Fig. 2(a)]. The prominent notches at about 20-Hz separation are due to interference between the direct arrival and its water surface ghost (i.e., $\Delta f = 1/\tau$, where τ is the ghost time delay, about 0.05 s in this case). For this same offset, the ghost time delay for the first bottom reflection will be larger, resulting in a smaller notch separation.

Conversely, the bubble-pulse period ($T_B \simeq 0.02$ s) is independent of travel path. The frequency domain bubble modulation will be mainly due to the first bubble pulse, resulting in a notch separation of roughly $\Delta f_B = 1/T_B = 50$ Hz. The notch modulation, at about 50-Hz separation, can be seen in the amplitude spectrum of the near offset bottom reflection shown in Fig. 2(b). In the absence of bubble pulses after the first, the position of the first notch would be at

$f = 1/2T_B \simeq 25$ Hz, the second at 75 Hz, etc. The effect of including the remaining bubble-pulse train is to shift the notch positions closer to zero. The modulation superimposed on the bubble-pulse modulation is, of course, due to the ghost delay.

Our debubbling technique involves bandpassing the seismograms to the lowest frequency band which is contained between two successive major bubble notches, in this case between about 10–60 Hz [Fig. 2(b)]. An autoregressive (AR) algorithm (Oldenburg *et al.*[7]; Walker and Ulrych[8]) is used to extend the frequency band toward both the lower and the higher frequencies (Appendix A). The extension process is based on the limited frequency information of the bandpassed data and does not see the original bubble-notch periodicity. Hence, it produces a relatively white spectrum corresponding to a seismogram in which the bubble-pulse train is suppressed.

As a simple example a short time window of the recorded seismograms [Fig. 3(a)] is used in which only the direct arrival and the ghost are present. Figure 3(b) shows the bandlimited (10–60 Hz) seismograms resampled at 1.333 ms, while the results of the spectral extension AR algorithm are shown in Fig. 3(c). As is clearly seen, the bubble-pulse effects are largely diminished.

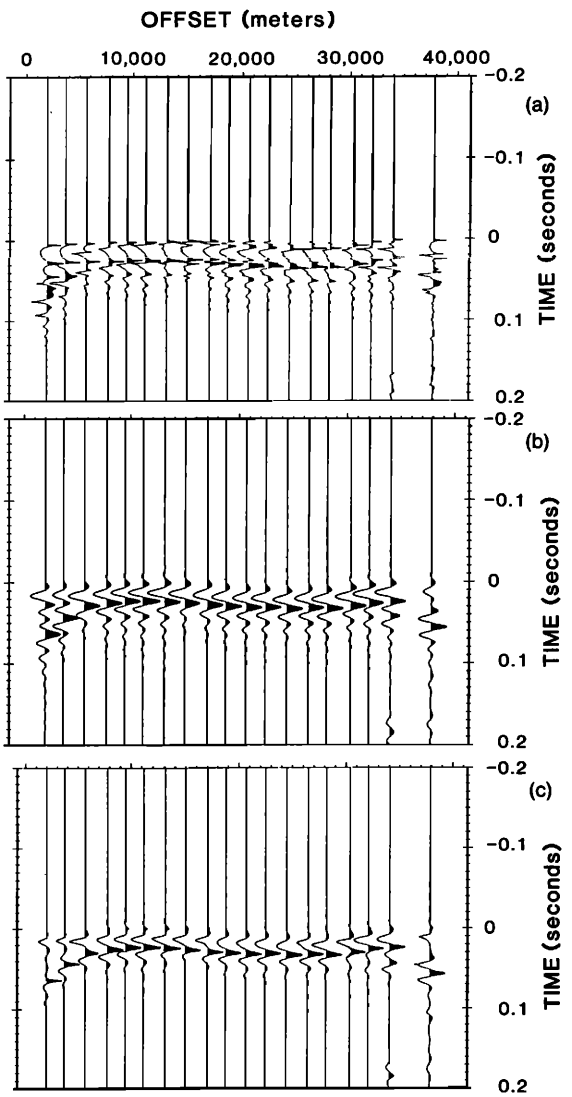

FIG. 3. (a) The original data, sampled at 0.667 ms, taken from a window aligned on the direct arrival. (b) The data in (a) after bandpass filtering (10–60 Hz), and resampling at 1.333 ms. (c) The data in (b) after application of the AR process.

The shallow portion of data following the first reflection from the sea floor (Fig. 1) was deconvolved using the processing procedure described above. Figures 4–6 show the input data, the bandpassed and resampled data, and the AR processed data, respectively. Although the final deconvolved results have simplified the overall appearance of the data and have delineated four distinct events in the time window 0–200 ms, the phase of the deconvolved output is considerably less consistent than that of the bandlimited data shown in Fig. 5. Consequently, having noted the locations of the four events delineated by the AR process, the bandpassed presentation is used for the actual picking of the travel time-offset ($T - X$) trajectories to be inverted.

The four time-offset trajectories $T(X)$ representing the events delineated by the AR deconvolution are shown in Fig. 5 and summarized in Table I.

III. STACKING TO INTERVAL SOUND-SPEED INVERSION

In this first inversion to obtain an interval sound-speed model, the travel time trajectories were interpreted by treating the events shown in Fig. 5 as reflections from sub-bottom layers. Under the assumption of a one-dimensional layered earth in which the relation $(V_{i+1} - V_i)/V_i \ll 1$ holds, the equation governing the travel time-offset $[T(X)]$ relations for the reflection from the ith layer interface is given by

$$T(X)_i^2 = T_{0i}^2 + X^2/V_i^2, \tag{1}$$

where T_{0i} is the two-way vertical travel time to the ith reflector, X is the source–receiver offset, and V_i is a weighted average sound speed from the surface to the ith reflector [known in the seismic industry as the stacking sound speed and assumed to be a good approximation to the quantity known as the root-mean-square (rms) sound speed (Aki and Richards[9])].

Dix[10] has shown that the relation between the layer interval sound speeds and the rms sound speeds is given by

$$V_{i\text{rms}}^2 = \frac{1}{T_{0i}} \sum_{j=1}^{i} v_j^2 \Delta t_j, \tag{2}$$

where Δt_j is the vertical incidence two-way travel time through the jth layer and v_j is the interval sound speed in the jth layer. In this section, Eq. (2) is used to estimate the interval sound-speed profile.

Two stable solutions to the integral representation of Eq. (2) have been presented in a recent publication by Oldenburg *et al.*[11] The first technique is based on Backus–Gilbert linear inverse theory and is designed to yield an interval sound-speed model which is a continuous function of depth. The second technique is a linear programming approach and is designed to yield a layered interval sound-speed model. A brief description of these techniques is given in Appendix B.

The first step in the inversion procedure is to obtain the rms sound speeds $V_{i\text{rms}}$ and the vertical two-way travel times

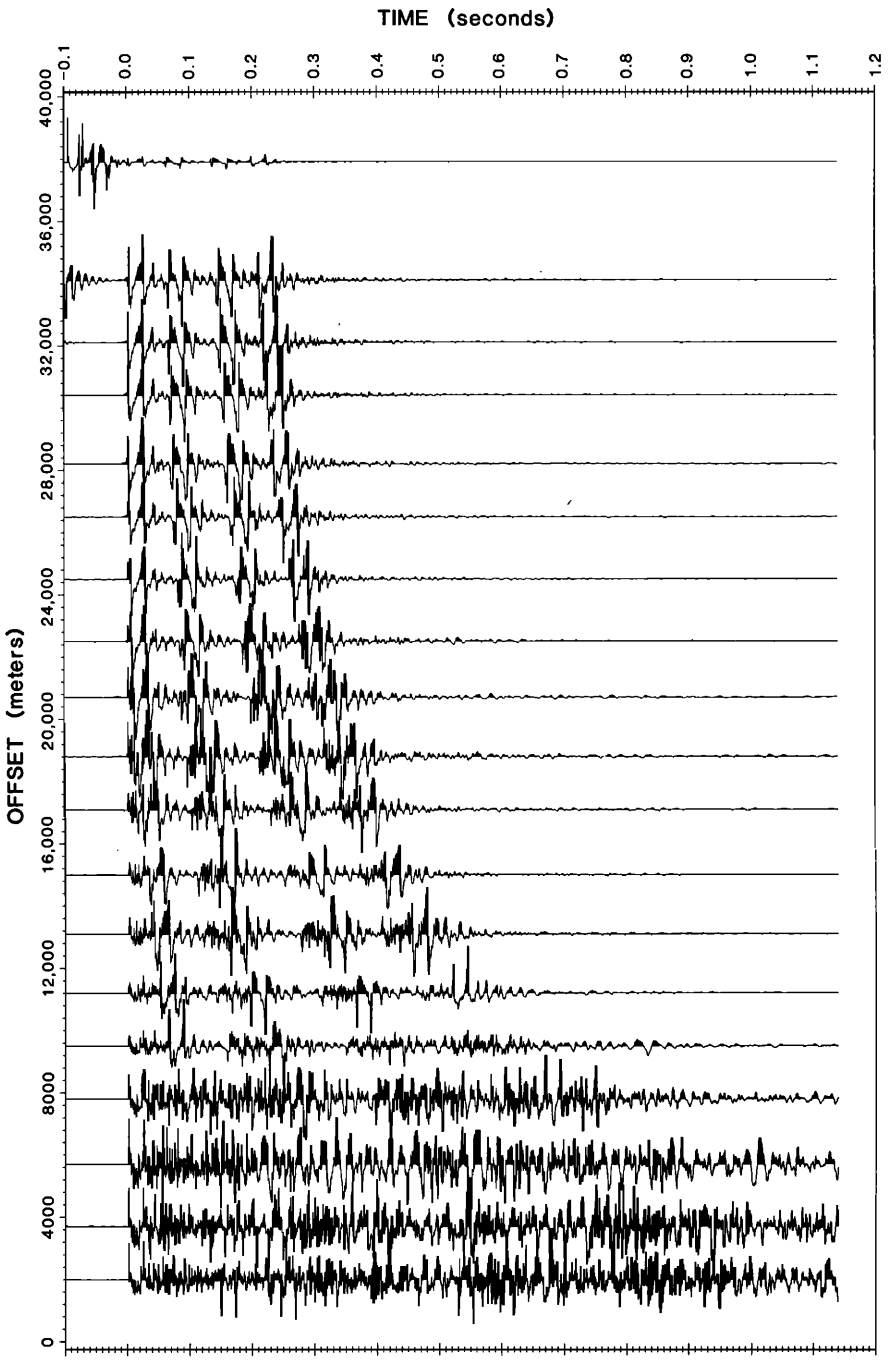

FIG. 4. The first 1.2 s of original data following the direct wave.

T_{0i} for each reflection trajectory. Using Eq. (1), the travel time data for each of the reflection trajectories summarized in Table I have undergone linear regression analysis (T^2 vs X^2) to estimate T_{0i}, $V_{i\text{rms}}$, and their associated standard deviations. These quantities are summarized in Table II. The first three rms sound speeds were then inverted using the methods mentioned above. Note that, because of its rms sound speed and the time separation $T_{04} - T_{01}$, the fourth trajectory was identified as a water surface multiple of the first bottom bounce, and was not included in the inversion.

The estimated interval sound-speed profiles, as a function of normal incidence two-way travel time, are shown in Fig. 7(a) (Backus–Gilbert approach) and (b) (linear programming solution). The depths z, corresponding to the two-way travel times, were computed using

$$z(t) = \frac{1}{2}\int_0^t v(t')dt'$$

and are also indicated in Fig. 7(a) and (b). Apart from the basic differences in model structure inherent in these construction algorithms, the results are quite consistent, with an average sediment sound speed of about 1650 m/s and an average sound-speed gradient over the first 100 m of 2.7 ± 0.2 s^{-1}. The differences in the shape of the sound-speed curves are due to the design of the respective algorithms and the underdetermined nature of the problem. In view of the detected reflection at the zero-offset time corresponding to event 2 (see Table II) and the very large gradient in the linear programming solution at this time, the linear programming model is probably the preferred one. This

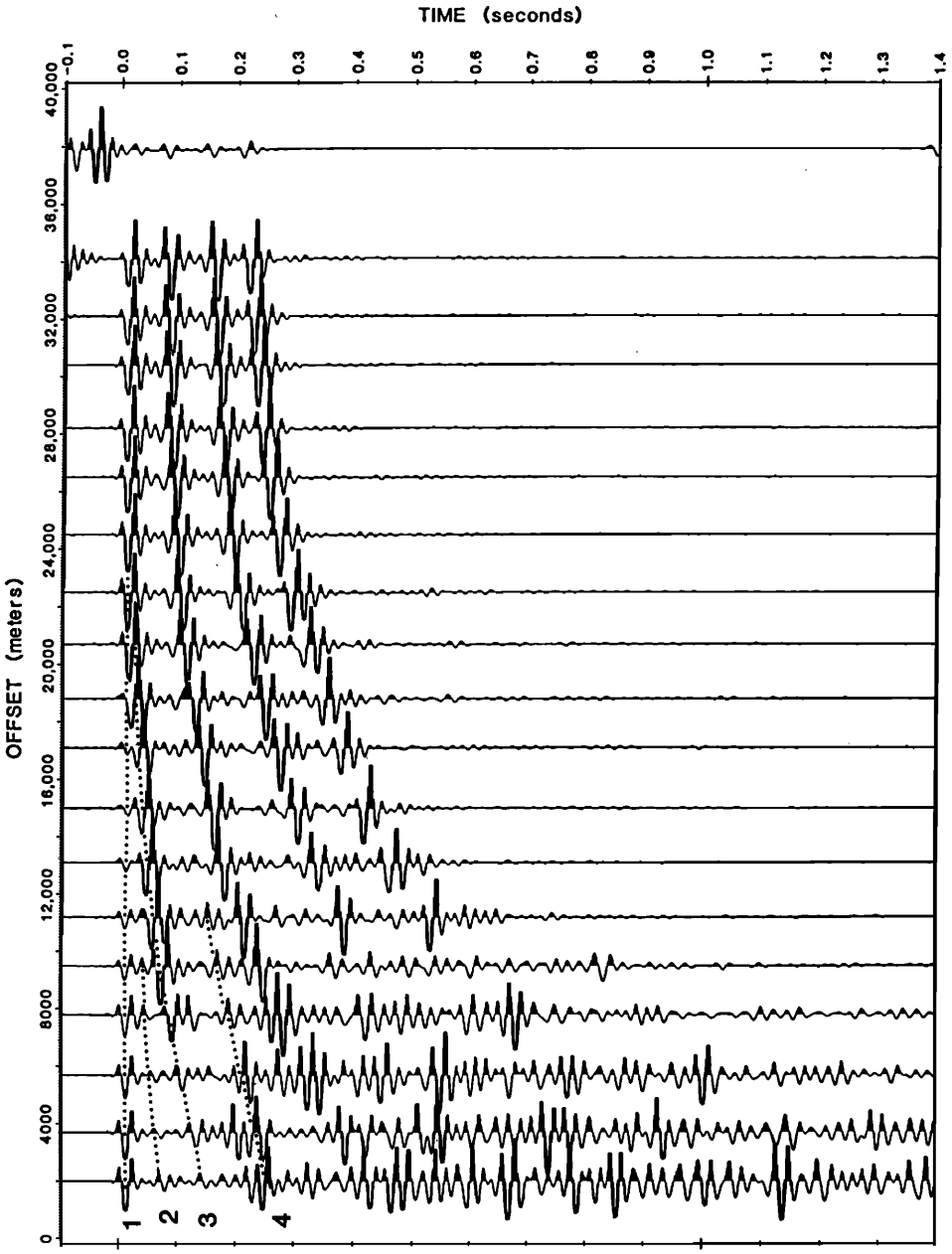

FIG. 5. The data as in Fig. 4 after bandpass filtering (10–60 Hz) and resampling at 1.333 ms. The marked events are summarized in Table I and are used in the sound-speed inversion.

model consists basically of two layers: a shallow layer about 50 m thick with an average sound speed of 1540 m/s, and an underlying layer with an approximate sound speed of 1760 m/s.

These results can also be compared with the profile obtained by Chapman *et al.*[1] using the simple interpretation that event 3 was a reflection from a constant sound-speed layer. The average sound speed determined in that work (1610 ± 50 m/s over the first 100 m) is consistent with the present results.

IV. RAY PARAMETER–INTERCEPT TIME ($p - \tau$) SOUND-SPEED INVERSION

In view of the large sound-speed gradients expected in the uppermost sediments, it is possible that the third event (Fig. 5), which was taken to be a reflection arrival in the analysis above, corresponds instead to a travel path of energy which was continuously refracted in its passage through the sediment layers. To assess the result of this interpretation, the arrivals of event 3 were treated as refractions, and subsequently inverted using the $p - \tau$ method of Garmany *et al.*[12] This procedure is outlined below, and discussed in more detail in Appendix C.

The inversion begins by transforming the $T - X$ trajectory of event 3 into the $p - \tau$ domain. In this work we have used a cubic spline to obtain $p = dT/dX$ (which is the ray parameter $\sin\theta/v$ in a one-dimensional earth), and then calculated the intercept time τ using the relation $\tau = T - pX$. The plot of the trajectories of the first and third events in the $p - \tau$ domain is shown in Fig. 8(a). The p value at the intersection of two events corresponds to the critical angle arrival at the respective interface, and hence may be directly translated into the sound speed of the lower layer. In this case the $p - \tau$ trajectory of the intermediate layer is missing, but the sound speed of the lowest layer can still be estimated

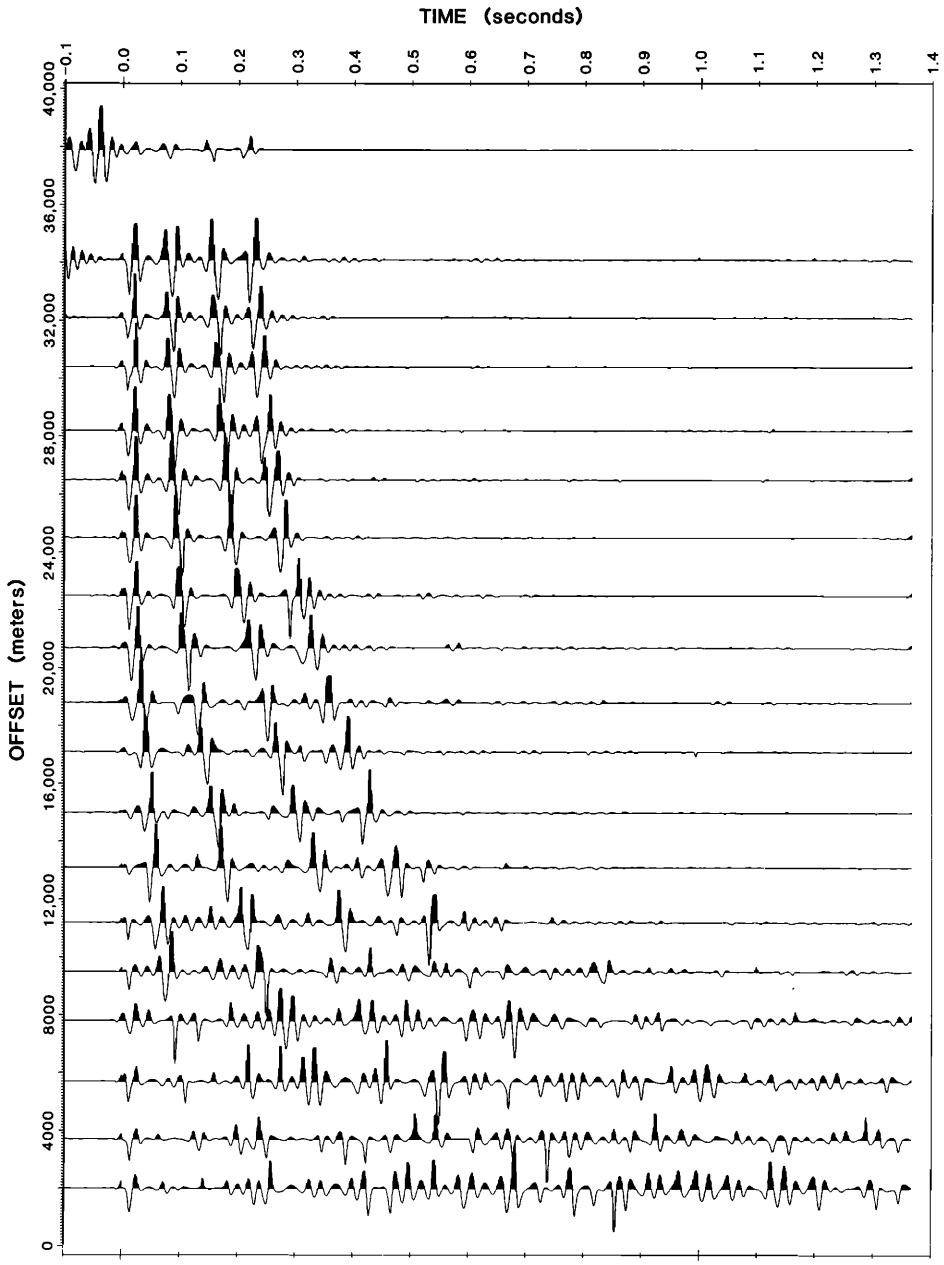

FIG. 6. The data as in Fig. 5 after application of the AR process.

to be 1650 ± 100 m/s.

The intercept time $\tau(p)$ and the ray parameter p for a layered earth model are related via the relation

$$\tau(p) = 2\int_0^{Z_p} [u(z)^2 - p^2]^{1/2}\, dz, \tag{3}$$

where Z_p is the turning depth for the ray that left the source with the ray parameter p and $u(z)$ is the wave slowness (i.e., reciprocal sound speed) at depth z.

With the assumption that sound speed increases monotonically with depth, and using a change of variables from depth (z) to slowness (u), Eq. (3) can be transformed into

$$\tau(p) = 2u_{\max}\int_p^1 m(u)(u^2 - p^2)^{1/2}\, du, \tag{4}$$

with $m(u)$ defined by $-dz(u)/du$ and the above monotonicity implying that $u_{\max} = \{1/[v(z=0)]\}$. Equation (4) can be solved by a variety of methods. However, since $m(u)$ is required to be positive, the problem is readily addressed using a linear programming technique.

Before proceeding with the $p-\tau$ inversion the intercept travel time portion τ of the water column, that is, the vertical component of the travel time through the water, is removed. The details of this layer stripping operation are given in Shultz[13] and a short description of the operation is found in Appendix C. The end result is a $p-\tau$ curve [Fig. 8(b)] simulating the case where both source and receiver have been placed on the ocean bottom.

The results shown in Fig. 9 are obtained by inverting the data of Fig. 8(b) using the Garmany method. It appears that the inverted refraction trajectory does not necessarily require a single constant sound-speed gradient. As is shown in the example in Appendix C, had the data required a sound-speed gradient, the method would have been able to follow it reasonably closely. Instead, two distinct subdivisions of the sediment layer were delineated: (a) a 68-m-thick layer with

TABLE I. Arrival times for four picked horizons used in the rms and $p-\tau$ inversion procedures (see Fig. 5).

	Horizon number			
	1	2	3	4
x (km)	T (s)	T (s)	T (s)	T (s)
2.0	4.594	4.663	4.730	4.850
3.7	5.041	5.102	5.161	5.278
5.7	5.811	5.864	5.908	6.024
7.8	6.810	6.858	6.888	6.995
9.5	7.710	7.749	7.771	7.875
11.2	8.665		8.710	8.815
13.1	9.778		9.811	
15.0	10.924		10.952	
17.1	12.219		12.234	
18.8	13.282		13.290	

an average sound speed of 1515 m/s and (b) a 32-m-thick layer with an average sound speed of 1725 m/s.

The gradient observed in Fig. 9 for the first layer compares favorably with the constant sound-speed gradient of 1.1 s^{-1} estimated by Chapman *et al.*,[1] in which the third arrival was treated as a refracted event. In their work it is likely that the value obtained was strongly influenced by the shallow near surface gradient, since only large offset data were used.

V. COMPARISON OF SOUND-SPEED INVERSION RESULTS

The stacking to interval sound-speed inversions consider the observed $T-X$ trajectories to be reflection arrivals. They also assume that the measured stacking sound speeds constitute reasonable approximations to the rms sound speeds. This latter assumption tends to break down for data in which source–receiver offsets are comparable to or larger than the depth of the reflecting interface. In the model study here, the sediment layer is relatively thin, with a sound speed which is comparable to the sound speed of the water column. Consequently, we have assumed that the straight ray approximation needed for the estimation of the stacking sound speeds holds reasonably well over the offsets used. The models (Fig. 7) obtained from this inversion agree reasonably well with the one presented by Chapman *et al.*[1] (in which they treated arrivals as reflections from the bottom of a constant sound-speed layer).

Nevertheless, we recognize the possibility that event 3 in the data may actually correspond to refracted arrivals. With this possibility in mind, we have approached the inversion process using the $p-\tau$ inversion method described by Garmany *et al.*[12] The results of this inversion (Fig. 9) generally

TABLE II. Zero-offset times, rms sound speeds, and associated standard deviations determined from the picks shown in Table I.

	Horizon number			
	1	2	3	4
T_0 (s)	4.397	4.468	4.535	4.665
V_{rms} (km/s)	1.500	1.501	1.505	1.497
V_{rms} (km/s)	0.001	0.001	0.001	0.001

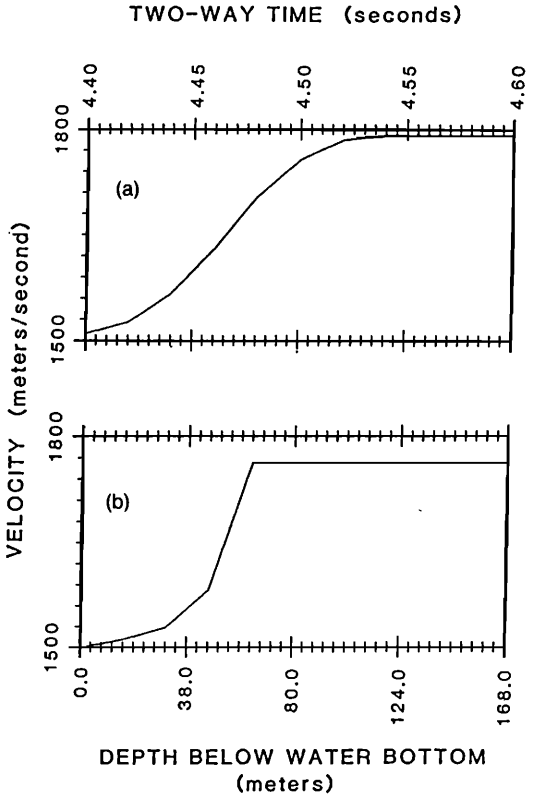

FIG. 7. (a) The Backus–Gilbert-inversion interval sound-speed profile. (b) The linear-programming inversion interval sound-speed profile.

agree with those of Fig. 7. However, clear differences in the details of the models exist. That is, although all models rise from a sound speed of 1.5 km/s to about 1.75 km/s at a depth of about 100 m, local sound-speed gradients differ substantially. Considering that the stacking sound-speed inversion used additional information contained in the data of event 2

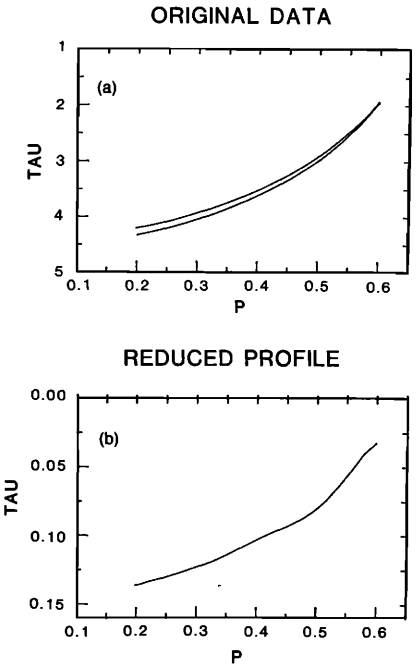

FIG. 8. (a) The $p-\tau$ trajectories of the first and third events. (b) The $p-\tau$ trajectory of the third event after "stripping" of the first event.

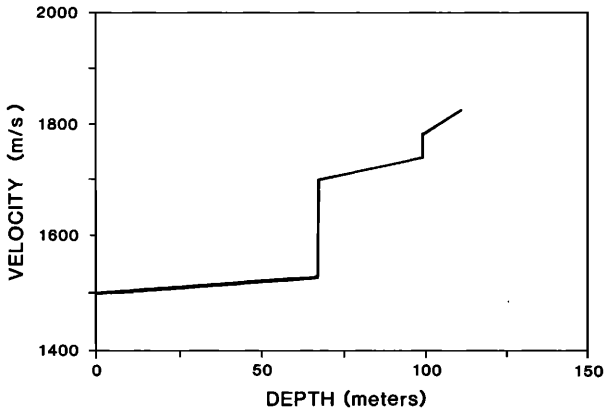

FIG. 9. The result of $p-\tau$ inversion on the data shown in Fig. 8(b).

and the excessive source–receiver offsets in the data, we anticipate that the results presented in Fig. 7 are somewhat biased toward higher sound speeds.

We conclude that the general agreement between all inversion results suggests that the data of event 3 consists of a mixture of both reflection and refraction arrivals. Since all inversions minimize the misfit to the observations, portions of the data set which do not fit well the preconceived assumptions of that inversion model will tend to be discounted in the final model, allowing a reasonable result. In other words, the best fit to the points as reflection data tends to discard the points which actually correspond to refraction arrivals, and vice versa.

VI. DENSITY AND SOUND-SPEED INVERSION—INVERSION OF PHASE-SHIFT INFORMATION

Postcritical reflections from a liquid–liquid interface undergo a phase shift which is dependent on the angle of incidence and on both the sound-speed and density contrast across the interface. Measured values of this phase shift for different angles of incidence can be used to determine the density and sound-speed ratios across the interface.

Consider an acoustic plane wave $p(x, z, t)$, propagating in some arbitrary direction defined by $\theta = \tan^{-1}(k_x/k_z)$, in a water column of constant depth. From the wave equation we have

$$p_R(x, z, t) = p_0 \exp[i\omega(t - \alpha_1 x - \beta_1 z)],$$

where $\alpha_1 = k_x/\omega, \beta_1 = k_z/\omega$, and k_x and k_z are the horizontal and vertical wavenumbers, respectively.

Let v_1 and v_2 represent the sound speed in the water and in the material underlying the water, respectively. Waves impinging at an angle of incidence $\theta > \theta_c$ (where θ_c is the critical angle) will, upon reflection, undergo changes in both the phase and amplitude (Rayleigh[14]; Arons and Yennie[15]).

For $\theta > \theta_c$ the reflected wave is expressed by

$$p_R(x, z, t) = r p_0 \exp[i\omega(t - \alpha_1 x + \beta_1 z) + i2\epsilon|\omega|/\omega],$$

with r the magnitude of the reflection coefficient and 2ϵ the associated phase change. The phase-shift angle ϵ depends upon the ratio of the densities and the ratio of the sound speeds of the two media. Explicitly,

$$\tan\epsilon = (\rho_1/\rho_2)[\tan^2\theta - (v_1/v_2)^2 \sec^2\theta]^{1/2}. \quad (5)$$

Consider an experiment in which a set of seismograms $S_k (k = 1,...,N)$ has been recorded at some small depth beneath the water surface. Analysis of the reflected waveforms of each seismogram will provide estimates of the phase-shift angle ϵ_k, while θ_k can be determined from the shot-receiver offset and the depth of the water column. The data set $\{\epsilon_k, \theta_k\}\, k = 1,N$ can be inverted to find estimates of ρ_2 and v_2 (as ρ_1 and v_1 of the water are known). This is done in the following manner. Equation (5) is rewritten as

$$\tan^2\epsilon_k = (\rho_1/\rho_2)^2 \tan^2\theta_k - (\rho_1 v_1/\rho_2 v_2)^2 \sec^2\theta_k \quad (6)$$

to obtain an equation which is linear in the variables $(\rho_1/\rho_2)^2$ and $(\rho_1 v_1/\rho_2 v_2)^2$. If $N > 2$, a least-square solution can be used to recover these variables and hence ρ_2 and v_2 can be obtained.

In practice, two limitations of Eq. (5) should be addressed. The first is that this expression is strictly true only for plane waves, and hence it is applicable only if the water bottom is many wavelengths away from the source. The second requirement is that the reflection interface be a liquid–liquid interface. Although this latter limitation seems severe in hard ocean bottom environments, the examples in Arons and Yennie[15] show that expression (5) is still an acceptable approximation.

In the analysis of the present data we have limited our attention to the four larger amplitude events in the second group of arrivals (the water column multiples or second bottom bounce arrivals), seen in Fig. 1 between times 1.3 and 3.3 s, and offsets 15 and 38 km. These arrivals were chosen because of their good signal-to-noise ratio. On the basis of the time separations and polarities of these events, it was concluded that they corresponded to reflections from a single internal interface in the sediments, but with different water path combinations (see Fig. 10). This was tentatively presumed to be the same interface responsible for event 3 used in the previous analyses.

The angular dependence $S(\theta)$ of the phase shift was estimated from this reflection data using the complex Karhunen–Loeve (CKL) transformation described in Appendix D. This analysis began by finding a suitable "reference," i.e., a farfield signature of a precritical signal for which there was no phase shift, in this case the first bottom bounce on the first offset trace. The phase differential between the refer-

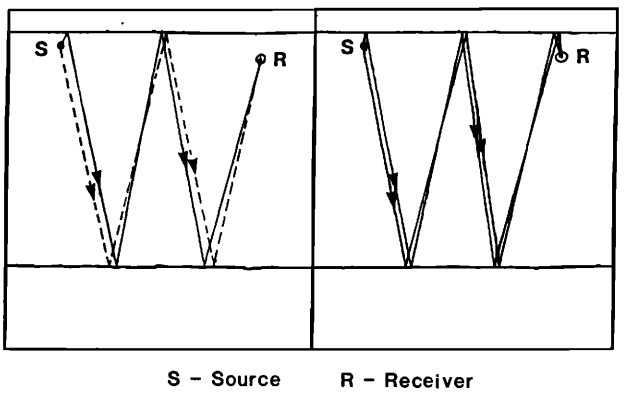

FIG. 10. Sketch of the longer ray paths of the four travel paths used in the phase-shift inversion.

TABLE III. Offset, angle of incidence θ, and phase angle (in rad) for the four reflections associated with the first multiple (see Fig. 1). The travel paths are illustrated in Fig. 10. All phases are relative to a precritical arrival. The phases have been halved because the multiple path has two reflections from the water bottom.

		First multiples Travel path number			
x (km)	θ (rad)	1 phase	2 phase	3 phase	4 phase
28.20	1.088	0.699	0.431	0.422	0.353
30.40	1.118	1.109	0.902	1.000	1.130
32.10	1.139	1.136	0.989	1.298	1.330
34.10	1.161	1.373	1.316	1.490	1.466
37.80	1.198	1.483	1.390	1.566	1.503

ence and each of the postcritical signals was then determined as shown in Appendix D. These differential phases, summarized in Table III, constitute components of the angular dependence function $S(\theta)$ required in the solution of Eq. (6).

An example of this operation for the first of the reflection events is shown in Fig. 11, where the data shown are taken from a 100-ms window enclosing the analyzed waveform for the different offset traces. Shown are: (a) the reference signal and six postcritical reflections (from offsets 25–38 km), (b) the envelopes of the analytic signals of the seven waveforms, and finally, (c) the reference and the six postcritical wavelets after phase rotation to the reference.

Using straight ray travel paths through the water column we have estimated the angles of incidence for each of the offsets present in the analyzed data sets (see Table III). Equation (6) was then solved, minimizing the square of the errors $\Sigma_i (\epsilon_i^C - \epsilon_i^O)^2$, where the superscripts C and O stand for "calculated" and "observed," respectively. The estimated sound-speed and density ratios for the water bottom sediments obtained from each of the analyzed data sets are given in Table IV. As well, Table IV contains estimates of v_2 that

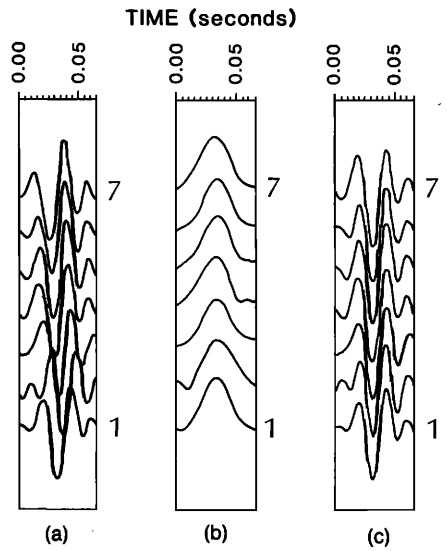

FIG. 11. (a) The precritical reference and six postcritical events picked from the first water bottom multiple. (b) The envelopes of the analytic traces of the events in (a). (c) The wavelets in (a) after phase rotation to the reference trace.

TABLE IV. Density and sound-speed ratios (ρ_2/ρ_1 and v_2/v_1) for the "second layer" (see the text) determined from inversion of the phases shown in Table III. Using the estimated sound-speed ratios and a sound speed for the "first layer" of 1.55 km/s, the sound speeds for the "second layer" were also estimated.

	First multiples Travel path number			
	1	2	3	4
Density ratio	1.23	1.17	1.00	1.12
Sound-speed ratio	1.17	1.14	1.15	1.16
Sound speed (km/s)	1.81	1.77	1.78	1.80

were obtained by supplying a value for v_1. Following the discussion of the sound-speed inversion results (Sec. V), and noting that the reflector horizon was tentatively identified as corresponding to event 3, the value of v_1 was set to 1.55 km/s.

VII. DENSITY EXTREMAL BOUNDS

When the sound speed v_2 beneath the reflecting interface is known, it is possible to obtain upper bound estimates of the corresponding density. We begin by rewriting Eq. (6) as

$$(\rho_1/\rho_2)^2[\tan^2\theta_k - (v_1/v_2)^2 \sec^2\theta_k] + e_k = \tan^2\epsilon_k, \quad (7)$$

where e_k denotes the error associated with the k th observation.

Approximate upper bounds to the density can then be found by specifying v_2 and using a linear programming scheme to minimize the objective function

$$\phi = \left(\frac{\rho_1}{\rho_2}\right)^2 + \sum_k |\epsilon_k|$$

subject to the constraint equation (7).

Using a sound-speed ratio v_2/v_1 of 1.16, we have solved the system of equations minimizing both the sum of the absolute value of the errors and the quantity ρ_1/ρ_2. The resultant upper bounds on the density ratios are summarized in Table V.

VIII. SUMMARY

Seismic data collected in the Alaskan Abyssal Plain has been analyzed to obtain estimates of some of the material properties of the shallow sea floor sediments. The first processing stage involved deconvolution of the bubble pulse by autoregressive extension of a limited portion of the Fourier spectrum of the data between the first two spectral notches caused by the bubble train. As the extension process does not

TABLE V. Upper bounds on the density ratios (ρ_2/ρ_1) for the "second layer" determined from inversion of the phases shown in Table III. The sound-speed ratio v_2/v_1 was constrained to be 1.16.

	First multiples Travel path number			
	1	2	3	4
Density ratio	1.29	1.44	1.19	1.22

see the bubble-notch periodicity, the bubble-pulse train is suppressed in the output seismogram.

The water bottom reflection and the three immediately following events delineated in Fig. 5 were picked for onset time to produce time-offset ($T-X$) trajectories for each of the four events. Presuming that these arrivals were reflections, linear regression of T^2 vs X^2 was performed to provide estimates of the vertical travel time at zero-offset (T_0) and of the rms sound speed (V_{rms}). These data were then inverted by two separate algorithms, a Backus–Gilbert approach and a linear-programming method, to produce time–sound-speed models, and after integration, depth–sound-speed models. The two models are in very good agreement, with an average sound-speed gradient over the first 100 m of 2.7 $\pm 0.2\ \text{s}^{-1}$.

Considering the possibility that the third event (Fig. 5) corresponded to a set of continuously refracted arrivals rather than reflected arrivals, this event was reinterpreted by a different approach. The process included conversion of the $T-X$ data of event 3 to $p-\tau$ data, followed by a layer stripping procedure to effectively place the source and receiver on the water bottom. The $p-\tau$ inversion of this reduced data set produced a depth–sound-speed model (see Fig. 9) which was similar to that of the previous linear programming inversion, where all arrivals were presumed to be reflection events.

The final results extracted from the data were the sound-speed and density ratios across an internal layer interface (tentatively identified as corresponding to event 3). The complex Karthunen–Loeve transformation was used to estimate the phase shift versus offset function for a number of postcritical reflections. Solving for both the sound speed of the underlying layer (with the top layer sound speed set to 1.5 km/s) and the density ratio across the interface resulted in estimated values of about 1.79 km/s and 1.14, respectively. Repeating the inversion with the sound-speed ratio fixed to be 1.16 resulted in an estimated upper bound on the density ratio of about 1.29 across the interface.

APPENDIX A: SPIKING DECONVOLUTION OF BANDLIMITED DATA

The problem of obtaining a sparse-spike representation of bandlimited reflection seismograms has been treated recently by a number of authors in the geophysical literature. The basic assumptions underlying this operation are as follows:

(a) The earth model consists of a set of physically distinct layers.

(b) The reflectivity series corresponding to the layered earth model is sparse, that is, reflections are generally separated by a number of zeros.

(c) The recorded seismogram is a reasonable bandlimited representation of the earth response function. That is, the phase and amplitude distortions of the source are largely removed.

The second assumption is expressed by

$$r(t)=\sum_{n=1}^{N} r_n \delta(t-n\Delta), \tag{A1}$$

where N is the number of samples in the input seismogram, r_n is the reflection coefficient at the nth sample, Δ is the sampling interval, and $\delta(t-n\Delta)$ represents a Dirac delta function at time $n\Delta$. The digital Fourier transform of a sparse reflectivity series $r(t)$ consists of the sum of a number of sinusoids and is written as

$$R(\omega_j)=R_j=\sum_{n=1}^{N} r_n \exp\left(\frac{-i2\pi jn}{N}\right), \tag{A2}$$

with j the index of ω, the angular frequency, and n the time sampling index.

It is obvious that each frequency in the series $R(\omega_j)$ contains contributions from each of the spikes present in the reflectivity series. Hence, it is expected that under the assumptions specified previously, a full-band estimate of the reflectivity function $r(t)$ can be obtained from an incomplete set of $R(\omega_j)$'s via the use of appropriate numerical techniques. The autoregressive technique which was used in this work will be described next.

1. Autoregressive (AR) deconvolution

As shown in Eq. (A2), the frequency representation of a sparse-spike series consists of a sum of a number of complex sinusoids each of which corresponds to a specific nonzero reflection coefficient. The problem of spectral extension can then be viewed as an autoregressive process where a complex prediction filter $\{\beta_k\}$ is calculated and the available information is extrapolated by a convolution with this filter. The process is simply summarized by the following set of equations.

Let the forward AR prediction be given by

$$R=\sum_{k=1}^{p} \beta_k R_{j-k}$$

and the reverse AR prediction by

$$R_j^*=\sum_{k=1}^{p} \beta_k R_{j+k}^*,$$

with p the order (length) of the prediction operator $\{\beta_k\}$ and * denoting the complex conjugate. We seek a prediction filter β such that the sum of the forward and reverse prediction errors is minimized in a least-square sense. That is, the filter coefficients are found through the minimization of

$$e^2=\frac{1}{N-p}\sum_{j=p+1}^{N}\left|R_j-\sum_{k=1}^{p}\beta_k R_{j-k}\right|^2 + \frac{1}{N+p}\sum_{j=1}^{N-p}\left|R_j^*-\sum\beta_k R_{j+k}^*\right|^2.$$

Details of some of the approaches to the solution of this minimization problem are given in Burg,[16] Ulrych and Clayton,[17] Ulrych and Bishop,[18] and Claerbout.[19]

The order of the prediction filter is quite important to a successful spectral extension process. Since one prediction coefficient is required for the extrapolation of each sinusoid, the ideal order of the AR process should be equal to or larger than the number of layers NL in the model. However, for bandlimited real data, where only $M<(N+1)/2$ frequency observations are given, the requirement $p>NL$ cannot be met. Hence, in this case, the process will usually detect only

the larger reflectors in the model, thereby reconstructing only the information concerning the major features of the sought reflectivity model. Our experience to date with a large number of synthetic, as well as real, data examples has proven the process to be quite successful. However, in cases where the local geology cannot be approximated by a relatively small number of reflectors, the AR process will have a somewhat lower likelihood of success.

APPENDIX B: STACKING TO INTERVAL SOUND-SPEED INVERSION

Given a set of N stacking sound speeds V_j, $j = 1,...,N$, with the corresponding errors δV_j, and possibly point estimates of the sound speed of some time intervals t_k, we would like to obtain an interval sound-speed model $v(t)$ which satisfies the given observations to within the specified errors.

Assuming that the given stacking sound speeds are a reasonable representation of the rms sound speeds, we write

$$V_j^2 = \frac{1}{t}\int_0^{b_j} v^2(t)\,dt$$

$$= \frac{1}{t_j}\int_0^{T_m} H(t_j - t)v^2(t)\,dt, \quad j = 1,...,N, \tag{B1}$$

with H the Heaviside step function and T_m representing the maximum two-way travel time in the desired model.

The set of linear equations in $v^2(t)$ specified in (B1) is underdetermined and admits infinitely many solutions. However, a specific model may be selected by minimizing a norm of the model subject to the data constraints. Two possible norms are

$$\Phi_1 = \int_0^{T_m} \left|\frac{d}{dt}[v^2(t)]\right| dt$$

and (B2)

$$\Phi_2 = \int_0^{T_m} \left|\frac{d}{dt}[v^2(t)]\right|^2 dt.$$

Minimization of either Φ_1 or Φ_2 will yield a minimum structure sound-speed curve since the integrated derivative is as small as possible. Spurious structure on the final model is therefore avoided.

Defining the model as $m(t) = d/dt[v^2(t)]$ and integrating Eq. (B1) by parts yield a set of new equations which are linear in $m(t)$. These are given by

$$V_j^2 - v^2(0) = \int_0^{T_m} \frac{1}{t_j}(t_j - t)H(t_j - t)m(t)dt, \quad j = 1,...,N. \tag{B3}$$

Additionally, when point sound-speed constraints are available (for example, from well-log information), it is possible to incorporate these into the solution. By integrating the model, the sound-speed value at time t_k can be written as

$$v^2(t) = v^2(0) + \int_0^{t_k} \frac{d}{dt}[v^2(t)]\,dt \tag{B4}$$

or

$$v^2(t_k) - v^2(0) = \int_0^{T_m} m(t)H(t - t)\,dt, \quad k = 1,...,M. \tag{B5}$$

Equations (B3) and (B5) are the final equations to be solved, where M and N are the number of point sound-speed constraints and stacking sound-speed picks, respectively.

1. Minimization of the norm Φ_2

Minimization of $\Phi_2 = \int m^2(t)\,dt$ subject to the data constraints is carried out using standard Backus–Gilbert techniques.

Letting e_j and G_j denote the jth observation and kernel, respectively, Eqs. (B3) and (B5) can then be rewritten as

$$e_j = \int_0^{T_m} G_j(t)m(t)\,dt, \quad j = 1,...,N+M. \tag{B6}$$

The constructed model will consist of a linear combination of the kernels $G(t)$:

$$m(t) = \sum_{i=1}^{N+m} \alpha_i G_i(t). \tag{B7}$$

Substituting (B7) into (B6) and exchanging the order of summation and integration we have

$$e_j = \sum_{i=1}^{N+M} \left\{\int_0^{T_m} G_j(t)G_i(t)\,dt\right\}\alpha_i, \quad j = 1,...,N+M,$$

which in matrix notation is written as

$$\mathbf{e} = \Gamma\boldsymbol{\alpha}. \tag{B8}$$

Consequently, the coefficients α necessary for the construction of the smallest model are obtained from Eq. (B8) as

$$\boldsymbol{\alpha} = \Gamma^{-1}\mathbf{e}. \tag{B9}$$

These equations are solved using standard spectral expansion techniques (Parker[20]). Importantly, the equations are not solved exactly so that the constructed model $m(t)$ fits the observations to within the given observational errors. More details and some applications of this and other construction techniques, including those steps which pertain to noise considerations, are given in Parker,[20] Oldenburg and Samson,[21] and Oldenburg *et al.*[22]

2. Minimization of the norm Φ_1

The minimization of Φ_1 subject to the data constraints is solved using linear programming techniques. We introduce the partitioning scheme $\{0 = t_0, t_1, ..., t_L = T\}$, and parametrize $m(t)$ such that it is a constant m_i, in the ith partition element. We then write Eq. (B6) as

$$e_j = \sum_{i=1}^{L} A_{ji}m_i, \quad j = 1,...,N+M, \tag{B10}$$

where

$$A = \int_{t_{i-1}}^{t_i} G_j(t)\,dt.$$

The minimization of the objective function

$$\Phi_1 = \sum_{i=1}^{L} |m_i|$$

subject to the constraints in (B10) yields the sought solution.

3. Discussion of the constructed models

The techniques discussed above solve for the model $m(t) = d/dt\{v^2(t)\}$, from which $v(t)$ is easily recovered. Although both methods are solving for the minimum structure model, there is a significant difference between the models generated by minimizing Φ_1 and Φ_2.

Minimization of Φ_2 yields a continuous interval sound-speed model $v(t)$. This model is particularly suitable for cases where the true sound-speed profiles are smooth and obey a continuous depth to sound-speed relation. However, if the true local geology is well approximated by a set of layers, the continuous sound-speed model will tend to follow the low-frequency sound-speed structure.

Minimization of Φ_1 yields a layered sound-speed model. This model resembles the one obtained by the Dix formula,[10] however, the technique described here is considerably more stable, and allows convenient handling of observational errors and the incorporation of additional knowledge in the form of sound-speed bounds or point sound-speed constraints.

APPENDIX C: THE ESTIMATION OF INTERVAL SOUND SPEEDS FROM $p-\tau$ TRAJECTORIES

Many of the processing and interpretative operations that are carried out on seismic data are performed more simply if the data are transformed into the $p-\tau$ (intercept time–ray parameter) domain. For any of the reflection and refraction trajectories in the $T-X$ (arrival time–offset) domain (see Fig. C1), the transformation would involve finding the slope of the tangent at all (T, X) points to get the ray parameter p:

$$p = \frac{dT}{dX} \tag{C1}$$

as well as finding the intercept time of the tangent line with the time axis:

$$\tau = T(X) - pX. \tag{C2}$$

An example of the procedure is shown in Fig. C2. Applying this transformation to the data in Fig. C1(b) results in the $p-\tau$ representation shown in Fig. C2(b).

Consider a plane wave propagating in a layered earth. As indicated in Fig. C3, the ray parameter p at any depth z is a constant equal to the sine of the propagation angle from vertical $[\theta(z)]$ divided by the sound speed at that depth:

$$p = \sin\theta(z)/v(z). \tag{C3}$$

Also shown is the conservation of the value of p along any refraction path, which is simply the manifestation of Snell's law.

The above gives the physical interpretation of the ray parameter p. As well, in Eq. (C2) the quantity T represents the total travel time of a ray (with ray parameter p) from the source to some arbitrary receiver location X. The quantity pX is the horizontal portion of T (see Fig. C3):

$$t_H(p) = \sum_i \left(\frac{2d_i}{v_i}\right)\sin\theta_i = p\sum_i 2d_i = pX.$$

Similarly, the intercept time τ is the vertical portion of T.

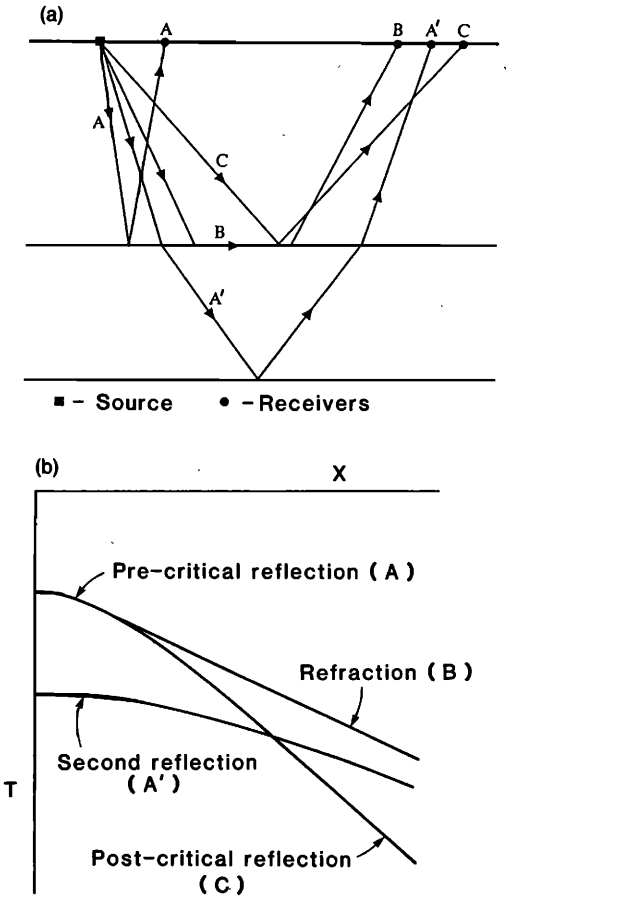

FIG. C1. Reflection and refraction arrivals from a single source measured in the $T-X$ domain. Ray paths are shown in (a) and the travel time curves are given in (b).

1. Layer stripping

The inversion of $p-\tau$ refraction data to obtain depth–sound-speed models (Garmany *et al.*[12]) presumes that both the source and receiver are on the surface of the layered earth. However, the layer stripping method of Shultz[13] allows one to place both the source and receiver at some arbitrary depth z (see Fig. C4) using a very simple operation.

For the sample ray path shown in Fig. C4(a) (where the path below layer 1 can be either a reflected or refracted path) one would like to adjust the data so it will be as if the source and receiver are on horizon 1. This involves having the source at S_1 and the receiver at R_1, as shown in Fig. C4(a). The new T and X values would be

$$T_{\text{new}} = T_{\text{old}} - t_1^a - t_1^b, \quad X_{\text{new}} = X_{\text{old}} - x_1^a - x_1^b, \tag{C4}$$

where the values of T_{old} and X_{old} are the travel time and offset, respectively, between S and R^b, and T_{new} and X_{new} are between S_1 and R_1 [see Fig. C4(a)]. The adjusted τ value would then be

$$\begin{aligned}\tau_{\text{new}} &= T_{\text{new}} - pX_{\text{new}} \\ &= T_{\text{old}} - (t_1^a + t_1^b) - p(X_{\text{old}} - x_1^a - x_1^b) \\ &= (T_{\text{old}} - pX_{\text{old}}) - (t_1^a + t_1^b) - p(x_1^a + x_1^b) \\ &= \tau_{\text{old}} - (t_1^a + t_1^b) - p(x_1^a + x_1^b).\end{aligned} \tag{C5}$$

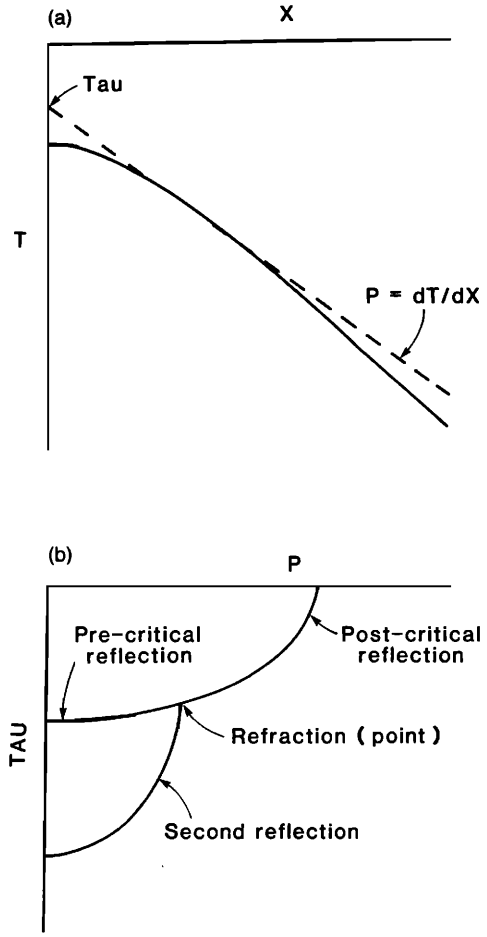

FIG. C2. (a) Tangent plane to $T-X$ trajectory to determine the slope p and intercept time τ. (b) The $p-\tau$ representation of the data shown in Fig. C1.

The second half of the right-hand side in Eq. (C5) is simply the intercept time corresponding to the reflection from horizon 1 (for a source at S and a receiver at R).

$$\tau_1 = t_1^a + t_1^b + p(x_1^a + x_1^b).$$

Thus to remove the effects of the travel path in layer 1 re-

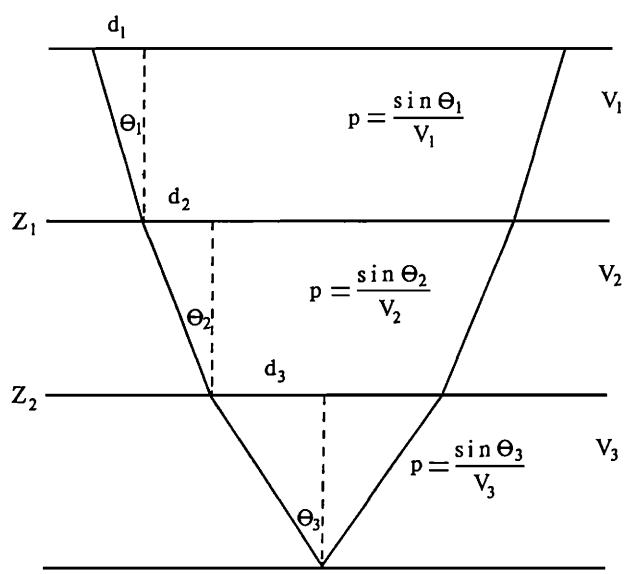

FIG. C3. Snell's law and the physical significance of p.

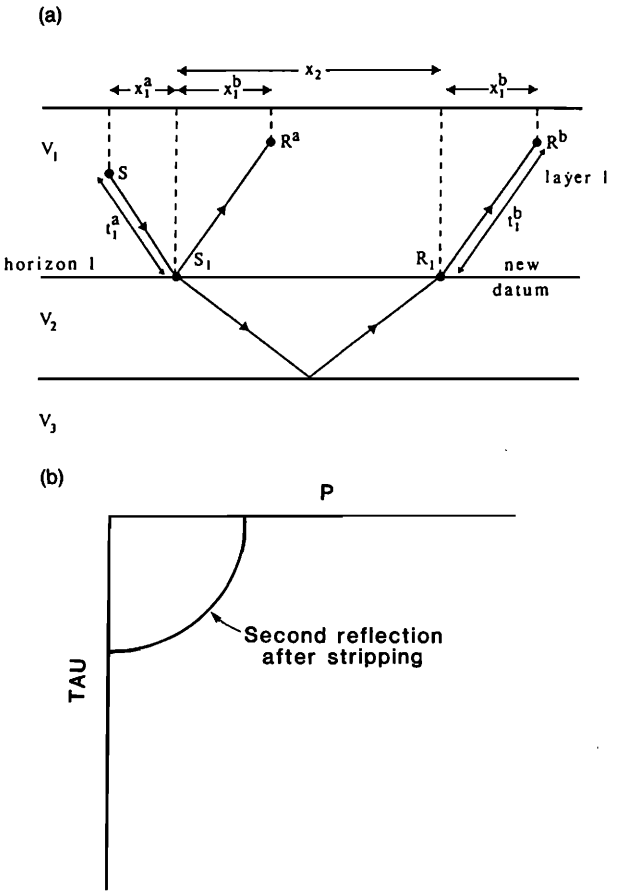

FIG. C4. (a) Travel paths involved in the layer-stripping method. (b) The $p-\tau$ data of Fig. C2(b) after stripping of the first layer.

quires only that the values of τ corresponding to this path be subtracted from the values of τ of the deeper horizons, for all values of p [see Fig. C4(b)].

This stripping operation can be continued progressively through the layers to move the new datum successively deeper.

2. $p-\tau$ inversion of travel time data

It is now appropriate to expand on the Introduction to outline the inversion procedure used here. Consider a one-dimensional earth in which the sound speed $v(z)$ is a monotonically increasing function of depth. A plane wave traveling in such a medium will be refracted according to Snell's law:

$$\sin(i)/v(z) = p = \text{const.}$$

If $v(z)$is a monotonically increasing function of z then the ray follows a path like that shown in Fig. C5.

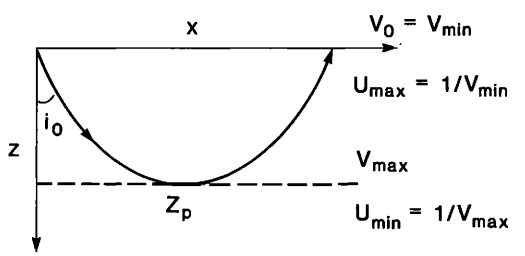

FIG. C5. Turning ray path considered for $p-\tau$ inversion.

The maximum penetration of a ray launched with an angle i_0 is given by z_p. At the turning point (or bottoming depth) z_p, the ray is moving horizontally so $i = \pi/2$ and

$$1/v(z) = p. \tag{C6}$$

3. Derivation of the travel time curves

Given a sound speed $v(z)$ we want to find the time it takes for the energy to arrive at a distance x from the source. The travel time equations are easily derived (Grant and West[23]). The basic equations are

$$\begin{aligned} t(p) &= 2\int_0^{z_p} \frac{dz}{v(1-p^2v^2)^{1/2}}, \\ x(p) &= 2\int_0^{z_p} \frac{pv\,dz}{(1-p^2v^2)^{1/2}}, \\ p &= \frac{dt}{dx} = \frac{1}{v(z_p)}. \end{aligned} \tag{C7}$$

It is helpful to think in terms of reciprocal sound speed $u(z) = 1/v(z)$. The quantity $u(z)$ is also referred to as the "slowness." In terms of reciprocal sound speed Eqs. (C7) become

$$\begin{aligned} t(p) &= 2\int_0^{z_p} \frac{u^2}{(u^2-p^2)^{1/2}}\,dz, \\ x(p) &= 2\int_0^{z_p} \frac{p}{(u^2-p^2)^{1/2}}\,dz. \end{aligned} \tag{C8}$$

By rearranging, we obtain

$$\begin{aligned} t(p) &= 2\int_0^{z_p} \left((u^2-p^2)^{1/2} + \frac{p^2}{(u^2-p^2)^{1/2}}\right) dz \\ &= px(p) + 2\int_0^{z_p} (u^2-p^2)^{1/2}\,dz. \end{aligned}$$

Therefore,

$$\tau(p) = t(p) - px(p) = 2\int_0^{z_p} (u^2-p^2)^{1/2}\,dz. \tag{C9}$$

Equation (C9) is the fundamental equation of interest. It expresses the relationship between the delay time τ and the quantities $u(z)$ and the bottoming depth z as a function of ray parameter p. Given a data set (t_i, p_i) $i = 1, N$, we would like to invert Eq. (C9) to find $u(z)$ and hence $v(z)$.

4. The linear transformation

Let us consider Eq. (C9). We observe that if values of τ at certain values of p are known, it is possible to invert those equations to obtain $u(z)$ and hence $v(z)$. We note, however, that Eq. (C9) is nonlinear and hence a model $u(z)$ could only be found through iteration. This is undesirable if it can be avoided.

Garmany *et al.*[12] showed how Eq. (C9) could be transformed into a linear equation, with the model the derivative of the bottoming depth with respect to the slowness.

It is assumed that there are no low sound-speed zones, that is, $v(z)$ is a nondecreasing function of z. Let $z = z(u)$. Then,

$$dz = \left(\frac{dz}{du}\right) du.$$

At the surface ($z = 0$), $u = u_{\max}$. At the bottoming depth ($z = z_P$), $u = u_{\min} = 1/v_{\max} = p$. Therefore, Eq. (C9) becomes

$$\tau(p) = 2\int_{u_{\max}}^{p} (u^2-p^2)^{1/2} \left(\frac{dz}{du}\right) du. \tag{C10}$$

5. Normalization of the equations

It is convenient to normalize the equations by a scale factor u (equal to the reciprocal of the surface sound speed). When both u and p are scaled by $u_{\max}$ Eq. (C10) is written as

$$\tau(p) = 2u_{\max}\int_1^p \left(\frac{dz}{du}\right)(u^2-p^2)^{1/2}\,du. \tag{C11}$$

The function $z(u)$ is a monotonically decreasing function of u and has the property that $z(1) = 0$. [Since $v(z)$ is monotonically increasing, $dv/dz > 0$ and hence $dz/du < 0$.]

Let $m(u) = -dz(u)/du$ be the new function to be determined. The final set of equations are

$$\begin{aligned} &\tau(p) = 2u_{\max}\int_p^1 m(u)(u^2-p^2)^{1/2}\,du, \quad m(u) \geqslant 0, \\ &\frac{dz(u)}{du} = -m(u), \quad z(u) = \int_1^u \left(\frac{dz(\xi)}{d\xi}\right) d\xi. \end{aligned} \tag{C12}$$

The solution to the set of Eqs. (C12) is easily effected through linear programming. A partition for u is introduced on the region $[u_{\min}, 1]$. Within each partition element the model $m(u)$ is assumed to be constant. The linear programming solution finds that set of m's such that

$$\phi = \sum_{i=1}^{s} m \tag{C13}$$

is minimized subject to the data constraints

$$\tau_j - \delta_j \leqslant \sum_{i=1}^{s} m_i a_{ij} \leqslant \tau_j + \delta_j, \quad j = 1,...,N, \tag{C14}$$

where $\tau_j = \tau(p_j)$, δ_j is the estimated error in τ_j and

$$a_{ij} = 2u_{\max}\int_{u_{i-1}}^{u_i} (u^2-p_j^2)^{1/2}\,du$$

is the integral of the jth kernel function over the ith partition element.

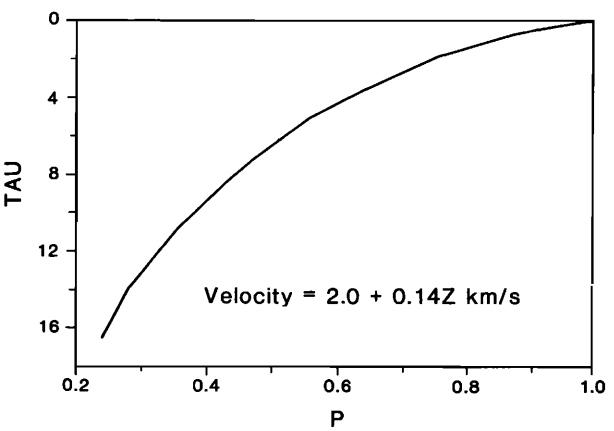

FIG. C6. The $p - \tau$ values for the synthetic model $v(z) = (2000 + 140z)$ m/s.

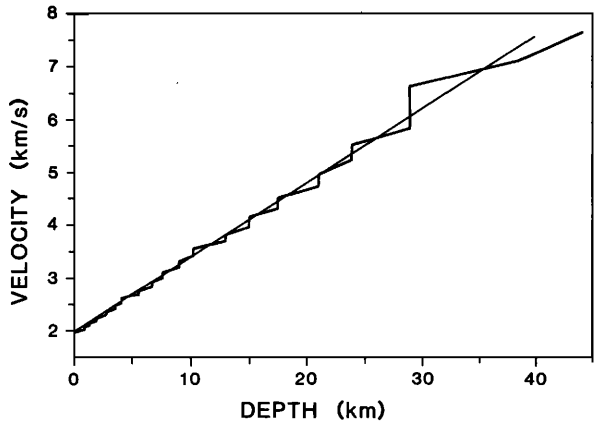

FIG. C7. The sound speed recovered from inversion of the data shown in Fig. C5, superimposed on the true sound-speed model.

The maximum number of nonzero values of m_i obtained from the linear programming solution will be N [the number of data in Eq. (C14)].

Having found $m(u)$, the next step is to compute $z(u)$:

$$z(u) = \int_1^u \left(\frac{dz(\xi)}{d\xi}\right) d\xi. \tag{C15}$$

The scale is now expanded (the normalization is undone) and $v(z)$ is recovered from $u(z)$.

We note that zeros in the initial solution require that $dz/du = 0$ over a range of u values. This requires that the sound speed changes but that z does not. Consequently, solution elements $m = 0$ correspond to sound-speed jumps in the earth.

The method outlined above is ideally suited to finding sound-speed models corresponding to a layered earth, but to illustrate that the method works well when the true sound speed is a linearly increasing function of depth, we present the following example. Consider a true sound speed $v(z) = 2.0 + 0.14z$ km/s. The $p - \tau$ values are shown in Fig. C6. The sound speed recovered from the $p - \tau$ inversion is shown in Fig. C7. Superposed upon that Fig. C7 is the true sound speed.

APPENDIX D: AN OVERVIEW OF THE KARHUNEN–LOEVE TRANSFORMATION

As pointed out in Ulrych *et al.*,[24] there are many ways in which the KL transformation can be derived. The work of Kramer and Mathews[25] is, however, very straightforward and insightful. We shall first present the essence of their paper, and then show its extension to complex signals.

Given a set of n real signals $e_j(t)$ and a $(m \times n)$ transformation matrix A with elements A_{ij}, Kramer and Mathews define a set of rotated signals

$$x_i(t) = \sum_{j=1}^{n} A_{ij} e_j(t), \quad i = 1,...,m, \ m \leqslant n. \tag{D1}$$

Let B be a $(n \times m)$ matrix which generates new signals:

$$\tilde{e}_i(t) = \sum_{j=1}^{m} B_{ij} x_j(t), \quad i = 1,...,n. \tag{D2}$$

If $\tilde{e}_i(t)$ is to be a good representation of the ith original signal, then the global misfit between the original and reconstructed signals, given by

$$\phi(m) = \sum_{i=1}^{n} \int |e_i(t) - \tilde{e}_i(t)|^2 \, dt \tag{D3}$$

must be acceptably small. For any $m \leqslant n$, Kramer and Mathews[25] showed that the matrices which minimized (D3) were $A = R^T$ and $B = R$. R is that orthogonal matrix which diagonalizes the inner product matrix Γ; the elements of Γ are

$$\Gamma_{ij} = \int e_i(t) e_j(t) \, dt = (e_i, e_j). \tag{D4}$$

Γ is symmetric and positive semidefinite, and hence is decomposable. $\Gamma = R \Lambda R^T$, where $\Lambda = \text{diag}(\lambda_1, \lambda_2, ..., \lambda)$ and the columns of R contain the normalized eigenvectors $\mathbf{r}$, where $\Gamma \cdot \mathbf{r}_j = \lambda \cdot \mathbf{r}_j$. When $A = R^T$, the rotated signals $x_j(t)$ form an n-dimensional subspace of a Hilbert space, and with these basis elements, the truncation error in Eq. (D3) is

$$\phi(m) = \sum_{i=m+1}^{n} \lambda_i. \tag{D5}$$

If the eigenvalues are arranged in descending order it follows that the first basis function can be used to reconstruct more of the total signal energy than any other basis function. For this reason, it is called the first principal component. Similarly, the second basis function will sometimes be referred to as the second principal component, etc.

The first principal component has an important characteristic. If $e_j(t) = c_j s(t)$, where c_j are real constants, and $s(t)$ is a given signal, then the first principal component will be

$$x_1(t) = \left(\sum_{j=1}^{n} c_j^2\right)^{1/2} s(t), \tag{D6}$$

that is, the first principal component will be a scaled version of the signal $s(t)$ and the complete set of input signal vectors $e_j(t)$ can be reconstructed from this basis vector and an appropriate set of weights. The remaining basis vectors $[x_i(t), i = 2,...,n]$ will be zero; they are not needed in the reconstruction.

These important characteristics of the KL transformation enumerated by Kramer and Mathews[25] for real signals carry over directly to the case when complex signals are used. For complex signals though, the inner product matrix is Hermitian and positive semidefinite and hence a unitary matrix is required for diagonalization. The eigenvalues will still be real, but the eigenvectors are complex. Nevertheless, the truncation error in Eq. (D3) is still given by Eq. (D5). Importantly, if $e_j(t) = c_j s(t)$, where the c_j are complex constants, then the first principal component will be

$$x_1(t) = \left(\sum_{j=1}^{n} |c_j|^2\right)^{1/2} s(t). \tag{D7}$$

Equation (D7) shows that complex signals which differ only by a complex scale factor can be represented by a single principal component.

As an illustration, we consider the following simple example. Let $e_1(t) = s(t)$ and $e_2(t) = \exp\{-i\epsilon\} s(t)$. Let $\|s\|^2 = (s, s^*)$ and $\Gamma_{ij} = (e_i, e_j^*)$, where $*$ denotes the complex conjugate. Thus

$$\Gamma = \|s\|^2 \begin{pmatrix} 1 & \exp\{i\epsilon\} \\ \exp\{i\epsilon\} & 1 \end{pmatrix}.$$

The eigenvalues of Γ are $\lambda_1 = 2\|s\|^2$, $\lambda_2 = 0$. The unitary matrix is

$$U = \frac{1}{2}\begin{pmatrix} 1 & -\exp\{-i\epsilon\} \\ \exp\{i\epsilon\} & 1 \end{pmatrix}. \quad \text{(D8)}$$

The first basis function is $x_1(t) = u_{11}\dagger e_1(t) + u_{21}\dagger e_2(t) = \sqrt{2}s(t)$, where u_{ij} are the elements of the first column of U and $\dagger$ denotes complex conjugate transpose.

The importance of these results to recorded seismograms is apparent when phase shifts of a source signal are considered. If $w(t)$ is the initial wavelet, a wavelet phase shifted by an amount ϵ is given by

$$w(t;\epsilon) = \cos\epsilon w(t) + \sin\epsilon\tilde{w}(t),$$

where $\tilde{w}(t) = H[w(t)]$ is the Hilbert transform (Aki and Richards[9]) of the initial wavelet. In such cases, it is expedient to consider the analytic signal (e.g., Bracewell[26]; Levy and Oldenburg[27]):

$$\hat{w}(t) = w(t) - i\tilde{w}(t).$$

The phase-shifted signal can be written as

$$w(t;\epsilon) = \mathrm{Re}[\hat{w}(t)\exp\{i\epsilon\}].$$

Let us consider a signal $e_1(t) = w(t)$ and another signal $e_2(t) = w(t;\epsilon)$. The corresponding analytic signals are

$$\hat{e}_1(t) = \hat{w}(t), \quad \hat{e}_2(t) = \hat{w}(t)\exp\{i\epsilon\}$$

and hence the signals are like those considered in the numerical example. Application of the complex KL (CKL) transformation will produce a first principal component equal to $\hat{w}(t)$. Moreover, Eq. (D8) shows that the phase rotation in the second signal is recoverable directly from the eigenvector associated with the first principal component. That is,

$$\epsilon = \tan^{-1}(u_{21}).$$

In this paper, the CKL transformation is applied to analytic seismograms. The ratio of the energy in the first principal component to the misfit energy using only one eigenvalue,

$$\chi = \lambda_1/\phi(1),$$

is used as a measure of correlation between the original set of signals. $\chi \gg 1$ implies a good correlation, whereas $\chi \simeq O(1)$ implies a poor correlation.

When $\chi \gg 1$, each of the original signals may be expressed (to within a small acceptable error) as a scaled and phase-shifted version of the first principal component. Phase shifts in the various signals can be estimated from the eigenvector associated with λ_1.

The properties outlined above suggest that the CKL algorithm can be very useful in investigating those physical phenomena that introduce phase shifts, which to a first order can be approximated by a constant. If the applicability of this model can be established, then estimation of the phases involved can yield useful information about earth properties.

[1]N. R. Chapman, I. Barrodale, and C. A. Zala, "Measurements of Sound-Speed Gradients in Deep-Ocean Sediments Using $L1$ Deconvolution Techniques," IEEE J. Oceanic Eng. **OE-9**, 26–30 (1984).

[2]R. L. Dicus and R. S. Anderson, "Effective Low-Frequency Geoacoustic Properties Inferred from Measurements in the North-East Atlantic," Naval Ocean Research and Development Activity, NORDA Rep. 21 (September, 1982).

[3]S. R. Santaniello, F. R. Di Napoli, K. W. Dullea, and P. D. Herstein, "Studies on the Interaction of Low Frequency Acoustic Signals with the Ocean Bottom," Geophysics **44**, 1922–1940 (1979).

[4]N. R. Chapman, "Modeling Ocean Bottom Reflection Loss Measurements with the Plane-Wave Reflection Coefficient," J. Acoust. Soc. Am. **73**, 1601–1607 (1983).

[5]L. C. Wood, R. C. Heiser, S. Treitel, and P. L. Riley, "The Debubbling of Marine Source Signatures," Geophysics **43**, 715–729 (1978).

[6]S. Levy and R. M. Clowes, "Debubbling: A Generalized Linear Inverse Approach," Geophys. Prospect. **28**, 840–858 (1980).

[7]D. W. Oldenburg, T. E. Scheuer, and S. Levy, "Recovery of the Acoustic Impedance from Reflection Seismograms," Geophysics **48**, 1318–1337 (1983).

[8]C. Walker and T. J. Ulrych, "Autoregressive Recovery of the Acoustic Impedance," Geophysics **48**, 1338–1350 (1983).

[9]K. Aki and P. G. Richards, *Quantitative Seismology* (Freeman, San Francisco, 1980), pp. 167–180.

[10]C. H. Dix, "Seismic Velocities from Surface Measurements," Geophysics **20**, 68–86 (1955).

[11]D. W. Oldenburg, S. Levy, and K. J. Stinson, "RMS Velocities and Recovery of the Acoustic Impedance," Geophysics **49**, 1653–1663 (1984).

[12]J. Garmany, J. A. Orcutt, and R. L. Parker, "Travel Time Inversion: A Geometrical Approach," J. Geophys. Res. **84**, 3615–3622 (1979).

[13]P. S. Schultz, "A Method of Direct Estimation of Interval Velocities," Geophysics **47**, 1657–1671 (1982).

[14]Lord Rayleigh, *The Theory of Sound* (Dover, New York, 1945), Vol. 2, p. 85.

[15]A. B. Arons and D. R. Yennie, "Phase Distortion of Acoustic Pulses Obliquely Reflected from a Medium of Higher Sound Velocity," J. Acoust. Soc. Am. **22**, 231–237 (1950).

[16]J. P. Burg, "Maximum Entropy Spectral Analysis," Ph.D. thesis (Stanford Univ., Stanford, CA, 1975).

[17]T. J. Ulrych and R. W. Clayton, "Time Series Modelling and Maximum Entropy," Phys. Earth Planet. Int. **12**, 188–200 (1976).

[18]T. J. Ulrych and T. N. Bishop, "Maximum Entropy Spectral Analysis and Autoregressive Decomposition," Rev. Geophys. Space Phys. **13**, 183–200 (1975).

[19]J. F. Claerbout, *Fundamentals of Geophysical Data Processing* (McGraw-Hill, New York, 1976), p. 274.

[20]R. L. Parker, "Understanding Inverse Theory," Ann. Rev. Earth Planet. Sci. **5**, 35–64 (1977).

[21]D. W. Oldenburg and J. C. Samson, "Inversion of Interferometric Data from Cylindrically Symmetric Refractionless Plasmas," J. Opt. Soc. Am. **69**(7), 927–942 (1979).

[22]D. W. Oldenburg, S. Levy, and K. P. Whittall, "Wavelet Estimation and Deconvolution," Geophysics **46**, 1528–1542 (1981).

[23]F. Grant and G. F. West, *Interpretation Theory in Applied Geophysics* (McGraw-Hill, New York, 1965).

[24]T. J. Ulrych, S. Levy, D. W. Oldenburg, and I. F. Jones, "Applications of the Karhunen–Loeve Transformation in Reflection Seismology," 53rd Annual SEG Meeting, Las Vegas, NV, Paper S6.5 (1983).

[25]H. P. Kramer and M. V. Mathews, "A Linear Coding for Transmitting a Set of Correlated Signals," presented at the 38th Annual SEG meeting in Denver, CO (1968).

[26]R. N. Bracewell, *The Fourier Transform and Its Applications* (McGraw-Hill, New York, 1978), 2nd ed.

[27]S. Levy and D. W. Oldenburg, "Deconvolution of Phase Shifted Wavelets," Geophysics **47**, 1285–1294 (1982).